



# Achromatic Quarter-Waveplate for the Terahertz Frequency Range Made by 3D Printing

Alexander Jäckel<sup>1</sup> · David Ulm<sup>2</sup> · Thomas Kleine-Ostmann<sup>2</sup> · Enrique Castro-Camus<sup>1</sup> · Martin Koch<sup>1</sup> · Jan Ornik<sup>1</sup>

Received: 15 June 2022 / Accepted: 24 August 2022 / Published online: 15 September 2022  
© The Author(s) 2022

## Abstract

Here we propose a 3D printed form-birefringent achromatic quarter-waveplate targeting the lower terahertz frequency range. The monolithically fabricated waveplate consists of three individual layers of different thickness and orientation of the stratified structure resulting in the achromatic response. The experimental results show that the performance of the fabricated waveplate fits the optimal behaviour within 5 % in terms of ellipticity and phase shift for frequencies between 75 GHz and 110 GHz.

**Keywords** Achromatic waveplate · Terahertz · 3D printing

## 1 Introduction

Since the late 1980s terahertz waves have encountered applications in many fields [1], such as probing quasi-particles in solid state physics [2] or the crystal structure of materials [3] among many others [4, 5]. Besides, many real-world applications for terahertz waves have emerged, such as telecommunications [6–8] and non-destructive inspection [9–11]. Most of the spectroscopic studies available have benefited from the capacity of the technique known as terahertz time-domain spectroscopy to detect both the amplitude and phase of the electromagnetic wave. Additionally, the polarization of the wave is a property that can be also used to probe important aspects of a sample, however, being rarely used [12]. The availability of optical components for terahertz waves is still relatively limited. Yet, a variety of 3D-printed devices to control the polarization of terahertz radiation have been demonstrated in the past

---

✉ Alexander Jäckel  
alexander.jaekkel@physik.uni-marburg.de

<sup>1</sup> Department of Physics and Material Sciences Center, Philipps-Universität Marburg, Renthof 5, 35032 Marburg, Germany

<sup>2</sup> Department High Frequency and Electromagnetic Fields, Physikalisch-Technische Bundesanstalt (PTB), Braunschweig, Germany

[13–18]. Furthermore, demonstrations of achromatic waveplates employing intrinsic material birefringence [19, 20] as well as form birefringence [15] have been reported.

The achromatic response can be obtained by stacking specific monochromatic wave plates along the propagation of the waves [19]. Thickness, birefringence and orientation of the individual waveplates defines the achromatic response of the final device and therefore needs to be carefully chosen. Previous demonstrations of terahertz achromatic waveplates include demonstrations of achromatic quarter waveplates (AQWP) employing intrinsically birefringent materials [19, 20] as well as 3D printed AQWP based on form birefringence [15]. In the former case, the achromatic response was obtained by optimizing the number of individual plates, their thickness, and relative orientation one to another. In the latter case, the form birefringence and thickness of two plates at a fixed relative orientation were optimized to obtain the achromatic response.

In this article, we present the design and experimental demonstration of a 3D printed AQWP, which is capable of evenly rotating the polarization of electromagnetic waves from 75 GHz to 110 GHz. We achieve this achromatic response by optimizing the number, thickness, and orientation of individual form birefringent plates taking also diattenuation into account. The optimized design consisting of three individual plates could be monolithically fabricated using a conventional 3D printer.

## 2 Design and Fabrication

The designed AQWP consists of a number of grating-like structures, which are sequentially printed along the optical axis into a single structure, as depicted in Fig. 1b and c. The individual gratings or stratified structures can be mathematically described as alternating material and air layers which form a periodically stratified media with a period  $\Lambda = a + b$  where  $a$  and  $b$  are the width of the material and air gaps, respectively. The obtained structure acts as a birefringent material with the fast and slow axis perpendicular and parallel to the structure, respectively. Figure 1a shows a schematic of the grating structure and the relative propagation direction of the incoming radiation. To obtain the frequency independent polarization change of the AQWP each grating must have a certain thickness  $d_i$  and relative orientation of the individual fast axes  $\psi_i$ .

We chose high impact polystyrene (HIPS) as 3D printing material, owing to its relatively good printability and high terahertz transparency [21]. For all samples we used a filling factor of 100 % and set the extrusion temperature as well as the heating bed temperature to 220 °C and 100 °C, respectively. Furthermore, we determined the permittivity of HIPS to be approximately  $\epsilon = 2.15$  with negligible dispersion and an absorption coefficient of approximately  $0.47 \text{ cm}^{-1}$  at 90 GHz. The 3D printer nozzle we used has a diameter of 400  $\mu\text{m}$ , which means that we were restricted to a stratification period of approximately 1150  $\mu\text{m}$  with an air gap width of 520  $\mu\text{m}$ . Therefore, we chose the lower end of the terahertz frequency range to avoid scattering, diffraction, and waveguiding effects [22].

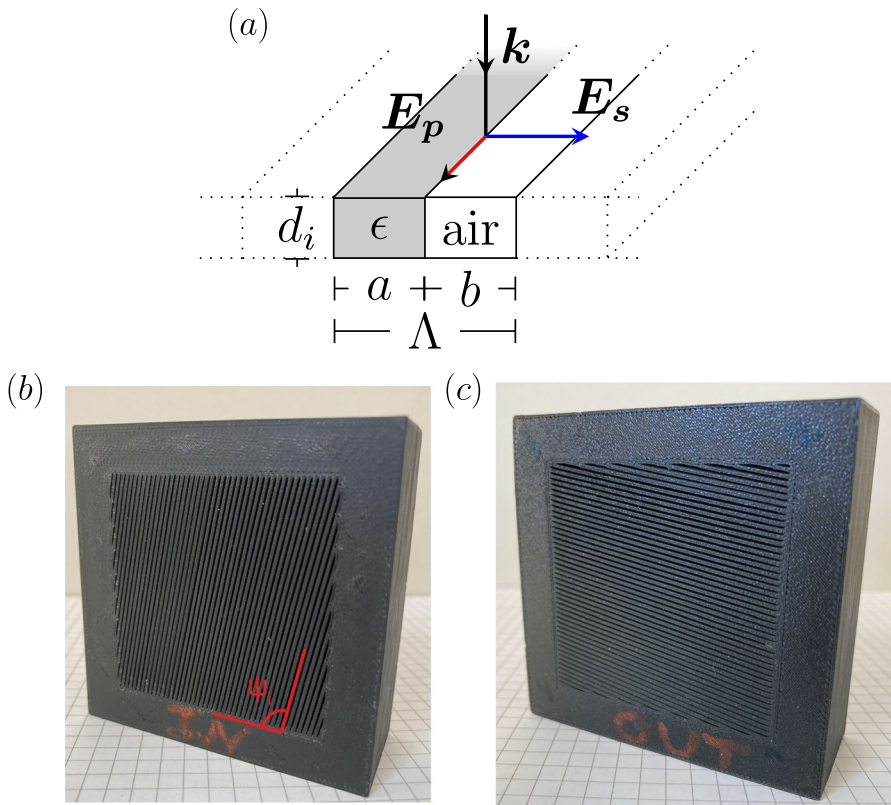


**Fig. 1** Schematic of the incident radiation on a grating (a), photos of the printed AQWP front- (b) and backside (c), which is based on the parameters shown in Table 1. Note the different orientations of the stratification. The functional square center part of the AQWP has an area of 25 cm<sup>2</sup>. The angle  $\psi_i$  is added for clarification, with  $i = 1$  since the front of the AQWP is shown. Each square of the grid paper has an area of 0.5 mm x 0.5 mm

The dielectric functions associated to form-birefringence which are based on the quasi-static effective medium theory [22] and can be written in form of the following two equations:

$$\epsilon_s = \frac{\epsilon\Lambda}{a + b\epsilon} \left( 1 + \frac{k^2 a^2 b^2}{12\Lambda^3} \frac{a\epsilon + b}{\epsilon^2} (\epsilon - 1)^2 \left( \frac{\epsilon\Lambda}{a + b\epsilon} \right)^2 \right), \tag{1}$$

and

$$\epsilon_p = \frac{a\epsilon + b}{\Lambda} + \frac{k^2 a^2 b^2}{12\Lambda^2} (\epsilon - 1)^2, \tag{2}$$

where  $k$ ,  $\epsilon_s$  and  $\epsilon_p$  denote the wavenumber, and the complex permittivities of the electric field perpendicular and parallel to the stratification, respectively.

Further details about the model can be found in the references [22–24]. Given these values of the stratification dimensions we calculate the expected form-birefringence to be approximately  $\Delta n \sim 0.086$  at 90 GHz. However, experimental characterization of a sample fabricated with such parameters revealed that the actual birefringence of the individual gratings was 0.119. This value was determined as an average birefringence of seven individually characterized samples of different thickness. The standard deviation of the birefringence of the seven samples was 0.002. Since by default the stratification layers were all printed in the same direction we considered that this could cause the additional 0.033 birefringence. To experimentally test this hypothesis we fabricated seven solid plates of different thickness and made the printer deposit each layer of the individual plates in the same direction. These plates were all printed without air gaps, which according to the theory mathematically represented by Eqs. 1 and 2 should show no form birefringence. However, the measurements of the solid plates showed an average birefringence of 0.039 and the standard deviation of 0.001. The obtained birefringence is similar to the difference between the calculated and measured birefringence of the actual stratified structure. Figure 2 shows the birefringence over the investigated frequency range, where the blue, black and red curves correspond to the birefringence of the stratified structure, the calculated birefringence and the birefringence of the solid plate, respectively.

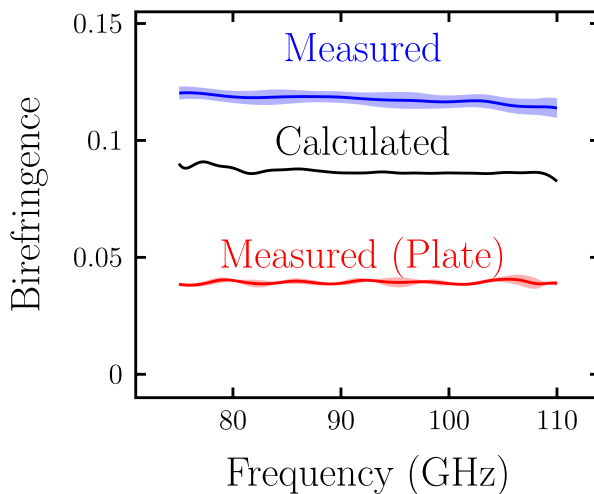


**Fig. 2** Curves from top to bottom: Measured birefringence of the grating structure, calculated form birefringence and measured birefringence of a full plate with all layers printed in the same direction. The form birefringence is calculated using Eqs. 1 and 2. In total 14 samples, seven full plates and seven samples with the grating structure, were printed and characterized. The measured curves and the surrounding shaded areas correspond to the mean and standard deviation of the measured birefringence of the seven samples, respectively. Note that the overall measurement uncertainty might have more contributions besides the measurement and fabrication repeatability, which is estimated by the standard deviation and represented by the shaded areas

We can describe the  $i$ -th individual grating of the AQWP by its corresponding Jones matrix  $\hat{J}_i$ :

$$\hat{J}_i(\psi_i, d_i) = \hat{Q}(-\psi_i)\hat{D}(d_i, \alpha_{s,p})\hat{R}_i(d_i, \Delta n)\hat{Q}(\psi_i), \quad (3)$$

where the  $2 \times 2$  complex matrices  $\hat{Q}$ ,  $\hat{D}$  and  $\hat{R}$  mathematically represent the relative orientation of the given grating, its diattenuation and its retardance, respectively. Furthermore,  $\alpha_s$  and  $\alpha_p$  denote the measured frequency dependent absorption coefficient along the perpendicular and parallel directions of the stratification, respectively. Finally the AQWP can be described by the non-commutative product  $\hat{J} = \prod_i^N \hat{J}_i$ , where  $N$  is the total number of individual gratings. Since the birefringence and diattenuation are taken from the measurement shown in Fig. 2a we end up with thickness  $d_i$  and orientation  $\psi_i$  as free parameters per grating, resulting in  $2N$  independent free parameters determining the design.

In case of an ideal quarter waveplate with its principal axes oriented at  $45^\circ$  with respect to the incident linearly polarized light, the transmitted light is circularly polarized. In this ideal case the first coefficient of the Jones vector representing the transmitted light will be purely real while the second coefficient will be purely imaginary; the ratio of these two will therefore be purely imaginary. Furthermore, in general for incident horizontally linearly polarized light the Jones vector of the transmitted light will have the following form:  $\mathbf{E} = (J_{11}, J_{21})^T$ , where  $J_{11}$  and  $J_{21}$  are the two complex entries in the left column of the  $2 \times 2$  complex Jones matrix  $\hat{J}$ . In the ideal case the ratio  $r = \frac{J_{11}}{J_{21}}$  should therefore be purely imaginary. This can be described by the loss function

$$L(\psi_1, \dots, \psi_N, d_1, \dots, d_N) = \sum \text{Re}(r)^2 + (1 - \text{Im}(r))^2, \quad (4)$$

where the summation is performed over the whole investigated frequency range.

By using the basin-hopping algorithm [20] to minimize  $L$  we obtain the optimized  $2N$  free parameters. The optimization was performed multiple times for  $N = 1, \dots, 5$  and we found that a design consisting of three individual gratings was sufficient for the targeted frequency range. The obtained parameters for the three gratings are shown in Table 1 and photos of the printed AQWP based on these parameters are shown in Fig. 1.

### 3 Experimental Characterization

For the characterization of the AQWP a quasi-optical system was used. This system consists of a commercial vector network analyzer (VNA) and different sets of waveguide frequency converters. From the available frequency ranges we chose the range from 75 GHz to 110 GHz, since it was the widest range in the lower end of the

**Table 1** Waveplate parameters for the design obtained via the optimization of  $L$  with  $N = 3$

Plate #	1	2	3	$\Sigma$
Thickness (mm)	14.14	13.11	7.00	34.24
Angle (deg)	246.54	171.27	38.65	

spectrum. The waveguide ports of the frequency extenders are connected to two rectangular horn antennas and as shown in Fig. 3 two off axis parabolic mirrors (OAPM) are used to reduce transmission losses [25]. Additionally, a high frequency resolution of 25 MHz was set on the VNA to be able to separate the signal from the initial pulse and the signal caused by standing waves. To characterize the AQWP we applied a slightly modified form of the measurement technique described in [19]. Since the emission pattern of the rectangular horn antennas is already linear we could perform the measurement using a single rotatable wire grid polarizer which was inserted between the AQWP and the detector in the beam path as shown in Fig. 3. Subsequently, the intensity  $I(\phi)$  of the radiation transmitted was measured for different angles  $\phi$  of the polarizer, which were varied in steps of  $10^\circ$ . We employ a Jones calculus description of the beam path to obtain the phase shift  $\delta$  and minor and major axes of the transmitted radiation denoted by  $A$  and  $B$ , respectively. In general the Jones vector  $\mathbf{E}_{wp}$  representing the polarization state after the AQWP can be written as follows:

$$\mathbf{E}_{wp} = A \cos(\omega t)\mathbf{x} + B \cos(\omega t + \delta)\mathbf{y}, \tag{5}$$

where the unit vector  $\mathbf{x}$  is parallel to the initially linearly polarized radiation and  $\mathbf{y}$  is perpendicular to it. The final state  $\mathbf{E}_f$  representing the measured signal is then given by the following:

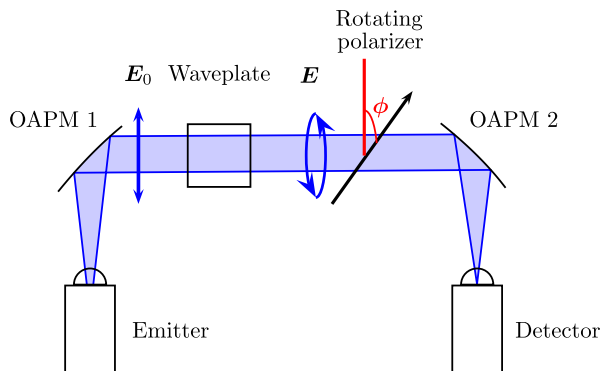
$$\mathbf{E}_f = \begin{pmatrix} 1 & 0 \\ 0 & 0 \end{pmatrix} \hat{Q}(\phi) \begin{pmatrix} 1 & 0 \\ 0 & 0 \end{pmatrix} \hat{Q}(-\phi)\mathbf{E}_{wp}. \tag{6}$$

Evaluating this matrix product we see that the intensity of the final field at the detector can be written as follows:

$$\sqrt{I(\phi)} = \sqrt{\mathbf{E}_f \mathbf{E}_f^\dagger} = |\cos(\phi)| [(A \cos(\phi) + B \sin(\phi) \cos(\delta))^2 + (B \sin(\phi) \sin(\delta))^2]^{1/2}. \tag{7}$$

Since the measurement is performed in steps of  $10^\circ$  it leads to 36 individual measurements which are subsequently normalized with respect to the measurement where the polarizer and polarization plane of the detector are parallel. For a

**Fig. 3** Schematic of the experimental setup. The rotating polarizer is removed for birefringence measurements



given frequency we fit the three parameters  $A$ ,  $B$  and  $\delta$  to the measured intensity as a function of  $\phi$ .

Figure 4a shows the measured phase shift and the values we calculated based on the design parameters and the measured birefringence. In case of an ideal quarter waveplate the phase shift equals  $\pi/2$ . The calculated and measured phase shift fit this value within a  $\pm 5\%$  range. Figure 4b shows the measured and calculated ellipticity (i.e., the ratio between minor and major axis of the polarization ellipse). In the ideal case for circularly polarized light we expect the two ellipse axes to be equal, therefore, resulting in an ellipticity of one. We account the deviation from optimal behaviour to a slight difference between the measured and the actual birefringence of the gratings. Additionally, the transmittance of the AQWP can directly be calculated as the sum of the squared minor and major axis of the polarization ellipse. Based on this calculation we find that the losses over the operational frequency range are below 3 dB.

## 4 Summary

In summary, we presented the viability of a 3D printed form birefringent AQWP. Our design consists of a single structure but can be understood and mathematically modelled as three individual form birefringent plates of different thicknesses combined at different orientation angles to form the AQWP. The set of thicknesses and orientation angles were determined through the optimization of a loss function which was based on the mathematical Jones calculus description of the three form birefringent plates. Furthermore, the experimental results match the performance of an ideal quarter waveplate within 5% for the frequency range between 75 GHz and 110 GHz. Finally, the design can be scaled to higher frequencies and a wider frequency range given a higher printing resolution of the 3D printer.

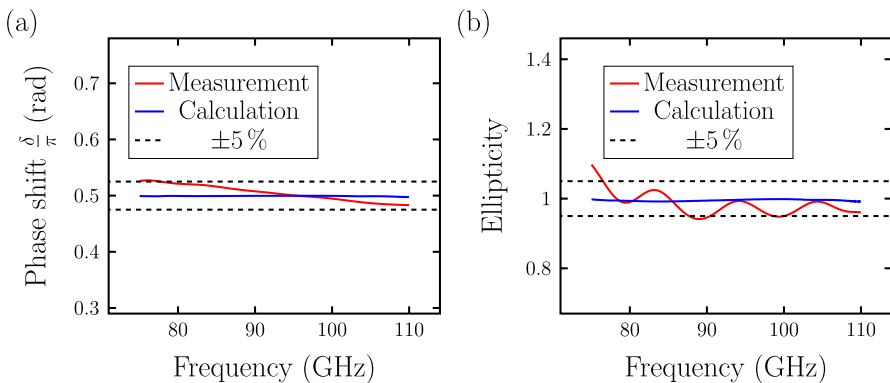


**Fig. 4** Measured and calculated (a) Measurement (red curve) and calculation (blue curve) result for the (a) phase shift, and (b) ellipticity, determined from design parameters in Table 1 and measured birefringence. The dotted lines indicate the  $\pm 5\%$  region within optimal performance

**Author Contribution** J.O. conceptualized the study with the support of M.K., and E.C. M.K., T.K., and E.C. provided the funding for the research. A.J. optimized the sample design and 3D printed the samples. D.U. performed the measurements and the evaluation with the help of T.K. A.J. processed the data and prepared the figures. All authors discussed and interpreted the results. The first manuscript draft was written by A.J. and E.C with subsequent input from all authors.

**Funding** Open Access funding enabled and organized by Projekt DEAL.

**Data Availability** Data will be made available upon a reasonable request.

## Declarations

**Ethics Approval and Consent to Participate** Not applicable

**Consent for Publication** Not applicable

**Competing Interests** The authors declare no competing interests.

**Open Access** This article is licensed under a Creative Commons Attribution 4.0 International License, which permits use, sharing, adaptation, distribution and reproduction in any medium or format, as long as you give appropriate credit to the original author(s) and the source, provide a link to the Creative Commons licence, and indicate if changes were made. The images or other third party material in this article are included in the article's Creative Commons licence, unless indicated otherwise in a credit line to the material. If material is not included in the article's Creative Commons licence and your intended use is not permitted by statutory regulation or exceeds the permitted use, you will need to obtain permission directly from the copyright holder. To view a copy of this licence, visit <http://creativecommons.org/licenses/by/4.0/>.

## References

1. H.J. Song, T. Nagatsuma, *Handbook of terahertz technologies: devices and applications* (CRC press, 2015).
2. R. Huber, F. Tauser, A. Brodschelm, M. Bichler, G. Abstreiter, A. Leitenstorfer, How many-particle interactions develop after ultrafast excitation of an electron–hole plasma, *Nature* **414**(6861), 286 (2001).
3. J. Ornik, L. Heidrich, R. Schesny, E. Castro-Camus, C.M. Keck, M. Koch, Non-destructive crystallinity assessment of indomethacin in tablets made from smartfilms®; using terahertz time-domain spectroscopy, *Scientific Reports* **12**(1), 1 (2022).
4. J.B. Jackson, J. Bowen, G. Walker, J. Labaune, G. Mourou, M. Menu, K. Fukunaga, A survey of terahertz applications in cultural heritage conservation science, *IEEE Transactions on Terahertz Science and Technology* **1**(1), 220 (2011).
5. F. Ellrich, M. Bauer, N. Schreiner, A. Keil, T. Pfeiffer, J. Klier, S. Weber, J. Jonuscheit, F. Friederich, D. Molter, Terahertz quality inspection for automotive and aviation industries, *Journal of Infrared, Millimeter, and Terahertz Waves* **41**(4), 470 (2020).
6. T. Kleine-Ostmann, T. Nagatsuma, A review on terahertz communications research, *Journal of Infrared, Millimeter, and Terahertz Waves* **32**(2), 143 (2011).
7. T. Kürner, D. Mittleman, T. Nagatsuma, *THz Communications: Paving the Way Towards Wireless Tbps* (Springer, 2022).
8. R. Shrestha, H. Guerboukha, Z. Fang, E. Knightly, D.M. Mittleman, Jamming a terahertz wireless link, *Nature Communications* **13**(1), 1 (2022).
9. J.P. Guillet, M. Roux, K. Wang, X. Ma, F. Fauquet, H. Balacey, B. Recur, F. Darracq, P. Mounaix, Art painting diagnostic before restoration with terahertz and millimeter waves, *Journal of Infrared, Millimeter, and Terahertz Waves* **38**(4), 369 (2017).



10. K. Krügener, J. Ornik, L.M. Schneider, A. Jäckel, C.L. Koch-Dandolo, E. Castro-Camus, N. Riedl-Siedow, M. Koch, W. Viöl, Terahertz inspection of buildings and architectural art, *Applied Sciences* **10**(15), 5166 (2020).
11. Y.H. Tao, A.J. Fitzgerald, V.P. Wallace, Non-contact, non-destructive testing in various industrial sectors with terahertz technology, *Sensors* **20**(3), 712 (2020).
12. D. Mittleman, J. Cunningham, M. Nuss, M. Geva, Noncontact semiconductor wafer characterization with the terahertz hall effect, *Applied Physics Letters* **71**(1), 16 (1997).
13. A. Hernandez-Serrano, E. Castro-Camus, Quasi-wollaston-prism for terahertz frequencies fabricated by 3d printing, *Journal of Infrared, Millimeter, and Terahertz Waves* **38**(5), 567 (2017).
14. A. Hernandez-Serrano, E. Castro-Camus, D. Lopez-Mago, q-plate for the generation of terahertz cylindrical vector beams fabricated by 3d printing, *Journal of Infrared, Millimeter, and Terahertz Waves* **38**(8), 938 (2017).
15. D. Rohrbach, B.J. Kang, T. Feurer, 3d-printed thz wave-and phaseplates, *Optics express* **29**(17), 27160 (2021).
16. A. Hernandez-Serrano, Q. Sun, E.G. Bishop, E.R. Griffiths, C.P. Purssell, S.J. Leigh, J. Lloyd-Hughes, E. Pickwell-MacPherson, Design and fabrication of 3-d printed conductive polymer structures for thz polarization control, *Optics express* **27**(8), 11635 (2019).
17. B. Scherger, M. Scheller, N. Vieweg, S.T. Cundiff, M. Koch, Paper terahertz wave plates, *Optics express* **19**(25), 24884 (2011).
18. J. Ornik, L. Gomell, S.F. Busch, M. Hermans, M. Koch, High quality terahertz glass wave plates, *Optics Express* **26**(25), 32631 (2018).
19. J.b. Masson, G. Gallot, Terahertz achromatic quarter-wave plate Jean-Baptiste, *Optics Letters* **31**(2), 265 (2006).
20. L. Wu, A. Farid, N.J. Laurita, T. Mueller, N.P. Armitage, A Compact Broadband Terahertz Range Quarter-Wave Plate, *Journal of Infrared, Millimeter, and Terahertz Waves* **41**(6), 642 (2020). <https://doi.org/10.1007/s10762-020-00686-2>.
21. S.F. Busch, M. Weidenbach, M. Fey, F. Schäfer, T. Probst, M. Koch, Optical Properties of 3D Printable Plastics in the THz Regime and their Application for 3D Printed THz Optics, *Journal of Infrared, Millimeter, and Terahertz Waves* **35**(12), 993 (2014). <https://doi.org/10.1007/s10762-014-0113-9>.
22. M. Scheller, C. Jördens, M. Koch, Terahertz form birefringence, *Optics Express* **18**(10), 10137 (2010). <https://doi.org/10.1364/oe.18.010137>.
23. S.M. Rytov, Electromagnetic properties of a finely stratified medium, *Soviet Physics JETP* **2**(3), 446 (1956).
24. D.K. Hale. The physical properties of composite materials (1976). <https://doi.org/10.1007/BF02403361>.
25. A. Kazemipour, M. Hudlička, S.K. Yee, M.A. Salhi, D. Allal, T. Kleine-Ostmann, T. Schrader, Design and Calibration of a Compact Quasi-Optical System for Material Characterization in Millimeter/Submillimeter Wave Domain, *IEEE Transactions on Instrumentation and Measurement* **64**(6), 1438 (2015). <https://doi.org/10.1109/TIM.2014.2376115>.

**Publisher's Note** Springer Nature remains neutral with regard to jurisdictional claims in published maps and institutional affiliations.